BrHgO• + C_2H_4 and BrHgO• + HCHO in Atmospheric Oxidation of Mercury: Determining Rate Constants of Reactions with Pre-Reactive Complexes and a Bifurcation

Khoa T. Lam, Curtis J. Wilhelmsen, Theodore S. Dibble*

Department of Chemistry, State University of New York-College of Environmental Science and Forestry, 1 Forestry Dr., Syracuse, NY, 13210, United States

ABSTRACT

Models suggest BrHgONO to be the major Hg(II) species formed in the global oxidation of Hg(0), and BrHgONO undergoes rapid photolysis to produce the thermally stable radical BrHgO•. We previously used quantum chemistry to demonstrate that BrHgO• can, like OH radical, readily abstract hydrogen atoms from sp^3-hybridized carbon atoms as well as add to NO and NO_2. In the present work, we reveal that BrHgO• can also add to C_2H_4 to form $BrHgOCH_2CH_2$•, although this addition appears to proceed with a lower rate constant than the analogous addition of •OH to C_2H_4. Additionally, BrHgO• can readily react with HCHO in two different ways: either by addition to the carbon or by abstraction of a hydrogen atom. The minimum energy path for the BrHgO• + HCHO reaction bifurcates, forming two pre-reactive complexes, each of which passes over a separate transition state to form a different products. Rate constants computed using Master Equation simulations indicate that hydrogen abstraction dominates over addition at atmospheric temperatures ($200\ \mathrm{K} \leq T \leq 333\ \mathrm{K}$) and pressures ($0.01\ \mathrm{atm} \leq P \leq 1\ \mathrm{atm}$). Subsequently, we compute the atmospheric fate of BrHgO• in a variety of air masses and find that BrHgOH formation via hydrogen abstraction will be the predominant fate (~70–99%), with the major competition (~20%) coming from addition to NO and NO_2 in polluted urban regions and stratospheric air. Given the absence of either field data on the identity of Hg(II) compounds or experimental data on the kinetics of BrHgO• reactions, the present manuscript should provide guidance to a range of scientists studying atmospheric mercury.

Submitted to *J. Phys. Chem. A* May 29, 2019

INTRODUCTION

Mercury (Hg) in the atmosphere exists primarily as gaseous elemental mercury (GEM, Hg(0)) due to its high equilibrium vapor pressure and low aqueous solubility.[1] Only after being oxidized to Hg(II) can mercury readily undergo deposition and enter aquatic ecosystems.[2,3] Here, oxidized mercury compounds are transformed into organic mercury compounds and bioaccumulate up the food chain, damaging human health globally due to their neurotoxic effects.[4] The rate and mechanism of mercury oxidation in the atmosphere are poorly understood, largely due to the near-absence of experimental kinetic data. This ignorance introduces large uncertainties in global and regional models of atmospheric mercury oxidation.[5–8]

Field and modeling studies implicate atomic bromine (Br•) as the species initiating oxidation of Hg(0) in bromine-rich environments, including the marine boundary layer and polar regions during the atmospheric mercury depletion events.[9–11] Furthermore, recent global models[9,12,13] assert that oxidation by Br•, alone, can account for the extent of global oxidation of Hg(II) in the atmosphere. Experimental[14] and theoretical studies[15–18] have confirmed the potential of Br• as an oxidant and determined the rate constants for the initiating step:

$$\mathrm{Br}\bullet + \mathrm{Hg} + \mathrm{M} \leftrightarrows \mathrm{BrHg}\bullet + \mathrm{M} \tag{1}$$

The subsequent chemistry of BrHg• remained relatively uncertain until recently. Given the high concentrations of HO_2 and, especially, NO_2, Dibble et al.[19] proposed that the addition of BrHg• to these radicals dominates the atmospheric fate of BrHg•:

$$\mathrm{BrHg}\bullet + \mathrm{NO_2} \rightarrow \mathrm{BrHgONO} \tag{2}$$

$$\mathrm{BrHg}\bullet + \mathrm{HO_2} \rightarrow \mathrm{BrHgOOH} \tag{3}$$

Indeed, using rate constants computed by Jiao and Dibble,[20] models which include these reactions have found improvements in model-measurement agreement of seasonal variations and deposition fluxes of mercury on both the regional[8] and global scales.[12] Notably, an extension of the CMAQ regional model[8] reproduced for the first time the diurnal pattern of a gaseous oxidized mercury (GOM, mostly Hg(II)) daytime maximum at a marine site. Although other reactions of BrHg• have been considered (addition to Br• and •OH,[15] addition to halogen oxides[19,21] and ROO•,[20] hydrogen abstraction from sp^3-hybridized carbons,[22] and addition to sp^2-hybridized carbons[22]), these reactions are much less important due to significantly lower reactant concentrations than NO_2 and HO_2,[12] or due to unfavorable reaction enthalpies (for hydrogen abstraction and addition). These results further highlight BrHgONO as the major Hg(II) species produced by the bromine-initiated oxidation of Hg(0).

Previous computational studies[23,24] identified the dominant fate of BrHgONO: it undergoes photolysis on a timescale of ~30 minutes. The photolysis produces NO and BrHgO•:

$$\mathrm{BrHgONO} + h\nu \rightarrow \mathrm{BrHgO}\bullet + \mathrm{NO} \tag{4}$$

BrHgO• has been theoretically calculated to possess strong bonds (60 kcal mol^{-1} and 70 kcal mol^{-1} for Br–Hg and Hg–O, respectively),[25] enabling it to react with trace gases before dissociating. Lam et al.[23]

computed rate constants for hydrogen abstraction by BrHgO• from CH_4 and C_2H_6 (reactions 5 and 6), and suggested rate constants for BrHgO• addition to NO and NO_2 (reactions 7 and 8).

$$\mathrm{BrHgO\bullet + CH_4 \rightarrow BrHgOH + \bullet CH_3} \tag{5}$$

$$\mathrm{BrHgO\bullet + C_2H_6 \rightarrow BrHgOH + \bullet C_2H_5} \tag{6}$$

$$\mathrm{BrHgO\bullet + NO \rightarrow BrHgONO} \tag{7}$$

$$\mathrm{BrHgO\bullet + NO_2 \rightarrow BrHgONO_2} \tag{8}$$

They concluded that abstractions of hydrogen atoms from alkanes are important globally, although additions to nitrogen oxides may compete in urban air masses. Nonetheless, their assessment of the fate of BrHgO• did not consider other plausible reactions, including reactions with oxygenated volatile organic compounds (VOCs) and unsaturated hydrocarbons.

In the present work, we use quantum chemistry to explore the reactions of BrHgO• with ethylene (C_2H_4) and formaldehyde (HCHO), which serve as model compounds for a range of olefins and carbonyl compounds:

$$\mathrm{BrHgO\bullet + C_2H_4 \rightarrow BrHgOCH_2CH_2\bullet} \tag{9}$$

$$\mathrm{BrHgO\bullet + HCHO \rightarrow BrHgOH + \bullet CHO} \tag{10a}$$

$$\mathrm{\rightarrow BrHgOCH_2O\bullet} \tag{10b}$$

We report potential energy profiles and rate constants for reactions 9 and 10. Additionally, we provide an assessment of the atmospheric fate of BrHgO•.

METHODS

The present study uses the same quantum chemistry methods as reported in our previous paper on BrHgO• reactions.[23] All quantum chemistry calculations were performed using Gaussian 09 revision D.01.[26] The standard Dunning correlation consistent basis set aug-cc-pVTZ[27,28] was used for hydrogen, carbon, and oxygen atoms. Calculations on Br and Hg atoms used the small-core Stuttgart/Cologne scalar relativistic pseudopotentials corresponding to the 10 and 60 innermost electrons of Br[29] and Hg,[30] respectively; a correlation-consistent augmented triple-zeta basis set[29,30] was used for electrons treated explicitly. References to this combination of basis set are simplified as AVTZ.

Unless specified, geometries of all stationary points (reactants, products, and saddle points) and all points along the minimum energy path (MEP) were optimized using the M06-2X functional.[31] Here, the MEP refers to the reaction path, whether mapped by the intrinsic reaction coordinate (IRC) calculation or by a relaxed scan of an internuclear distance. The optimizations and frequency calculations used a pruned "ultrafine" grid of 99 radial shells with 590 angular points per shell. The identities of local minima and transition states were verified based on the presence of all real harmonic frequencies and one imaginary frequency, respectively. For points along the MEP, projected frequencies for vibrations perpendicular to the MEP were computed. Zero-point vibrational energies (ZPE) and Gibbs free energies were computed using the harmonic oscillator and rigid rotor approximations with unscaled vibrational frequencies. Spin-unrestricted calculations were performed on open-shell species. Energies of all stationary points and selected points along the MEP were computed using the coupled cluster singles doubles and perturbative triples (CCSD(T)) method[32] along with the AVTZ basis set. CCSD(T) calculations only correlated electrons described by the atomic orbitals of Hg (5d6s), Br (4s4p), C (2s2p), O (2s2p), and H (1s). It should be noted that Gaussian 09 defaults to a different definition of the frozen cores of Hg and Br.

Due to the presence of pre-reactive complexes (PRCs) in both the BrHgO• + C_2H_4 and BrHgO• + HCHO systems, rate constants for these reactions were computed in two steps. In the first step, temperature-dependent rate constants of the PRC-forming step, $k^{\mathrm{VTST}}(T)$, were calculated in the high-pressure limit using variational transition state theory (VTST). $k^{\mathrm{VTST}}(T)$ corresponds to the minimum canonical rate constant, $k^{\mathrm{CTST}}(T)$, found along the MEP for forming the PRC, via:

$$k^{\mathrm{CTST}}(T) = (k_{\mathrm{B}}T/h)\exp(-\Delta G^{\dagger}(T)/\mathrm{R}T) \tag{11a}$$

$$k^{\mathrm{VTST}}(T) = \min_{\mathrm{s}} k^{\mathrm{CTST}}(s, T) \tag{11b}$$

where k_{B}, h, and R are the Boltzmann's constant, Planck's constant, and gas constant, respectively, $\Delta G^{\dagger}(T)$ is the molar Gibbs free energy of activation, and s is the position along the reaction coordinate.

To determine effective second-order rate constants $k([\mathrm{M}], T)$ as a function of number density of gas particles (pressure) and temperature, Master Equation simulations were carried out using the MultiWell Program Suite.[33,34] These simulations were initiated with chemically activated PRCs, whose initial energy distribution was convolved with k^{VTST} for the PRC-forming step. These PRCs were allowed to dissociate to isolated reactants or overcome barriers to form products. Microcanonical rate constants $k(\mathrm{E})$ were computed using Rice-Ramsperger-Kassel-Marcus (RRKM) theory. For both dissociation of PRCs, these rate constants were treated using the quasi-microcanonical approximation. In other words, the position of the canonical variational transition state was used to compute $k(\mathrm{E})$.[35,36] At each temperature and pressure simulated, we determined the fraction, $f([\mathrm{M}], T)$, of PRCs going on to react. Accordingly, $k([\mathrm{M}], \mathrm{T})$ is given by $k^{\mathrm{VTST}}(T) \times f([\mathrm{M}], T)$. Rate constants were computed for temperatures between 200 K and 333 K and pressures between 0.01 atm and 1 atm, covering the atmospheric conditions from ground level to the stratosphere. 1,000,000 simulations were carried out at each pressure and temperature to enable good precision ($\sigma < 1\%$). In these simulations, Lennard-Jones (LJ) parameters for species except for the bath gas N_2 were estimated as $\varepsilon/k_{\mathrm{B}} = 1.21 \times \mathrm{T_b}$, where $\mathrm{T_b}$ is the boiling point of the species, and $\sigma = 1.45\,(\sum \mathrm{V}_i)^{1/3}$, where V_i is the additive volume of the i^{th} atom in the species, and the summation being over all atoms in the species.[37] Here, we assume the boiling point of $HgBr_2$ (at 595 K) to be that of any species containing Br and Hg. All LJ parameters including those for N_2 are listed in the Supporting Information (**Table S3**). A single-exponential down model was used for energy transfer, with $\langle \Delta \mathrm{E_{down}} \rangle = 200\ \mathrm{cm^{-1}}$.

As implied by our use of RRKM theory, we assumed fast intramolecular vibrational relaxation (IVR) within the PRCs, as others have done.[38–41] Though unlikely, it seems reasonable to use this assumption for the first-ever study of these reactions. Accounting for IVR would require computationally demanding quasi-classical trajectory (QCT) calculations, and these calculations are not without their own limitations.

RESULT AND DISCUSSION

BrHgO• + C_2H_4 reaction. Figure 1 displays the potential energy profile for the BrHgO• + C_2H_4 reaction. The reaction proceeds by first forming a PRC before overcoming a small barrier to form $BrHgOCH_2CH_2$•. Although the M06-2X energy of the saddle point displays a 3.6 kcal mol^{-1} critical energy (relative to the PRC), CCSD(T) calculations indicate a saddle point submerged by 0.3 kcal mol^{-1}. Note that relative energies reported here are corrected for ZPE except where specified. However, CCSD(T) energies computed along the M06-2X reaction path revealed a positive critical energy relative to the PRC (by 0.5 kcal mol^{-1}) on the reactant side of the saddle point. This positive critical energy was used in the kinetics calculations. Energies along the path at both levels of theory are displayed graphically in the Supporting Information (**Figure S1**).

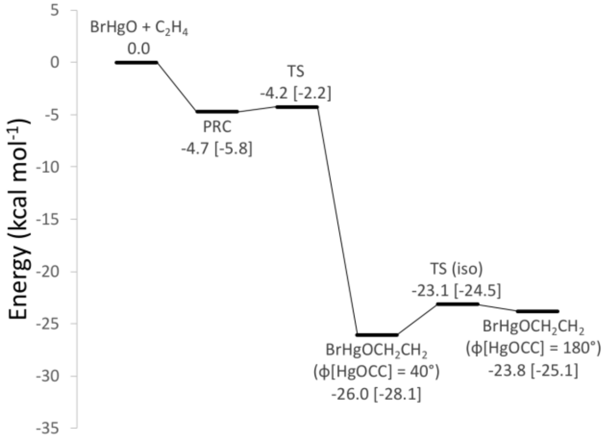

Figure 1. ZPE-corrected potential energy profile for the BrHgO• + C_2H_4 reaction at CCSD(T)//M06-2X/AVTZ. Values in brackets are energies at M06-2X/AVTZ.

The structures of reactants, products, and all saddle points of the reaction are displayed in **Figure 2**. There are two conformers of the product: a more stable adduct of C_1 symmetry with Φ[HgOCC] = 40° (termed folded), and another located 2.2 kcal mol^{-1} above the conformer of C_s symmetry with Φ[HgOCC] = 180° (termed extended). These structures are connected by a rotational saddle point (TS (iso)), which lies 2.8 kcal mol^{-1} above the folded conformer.

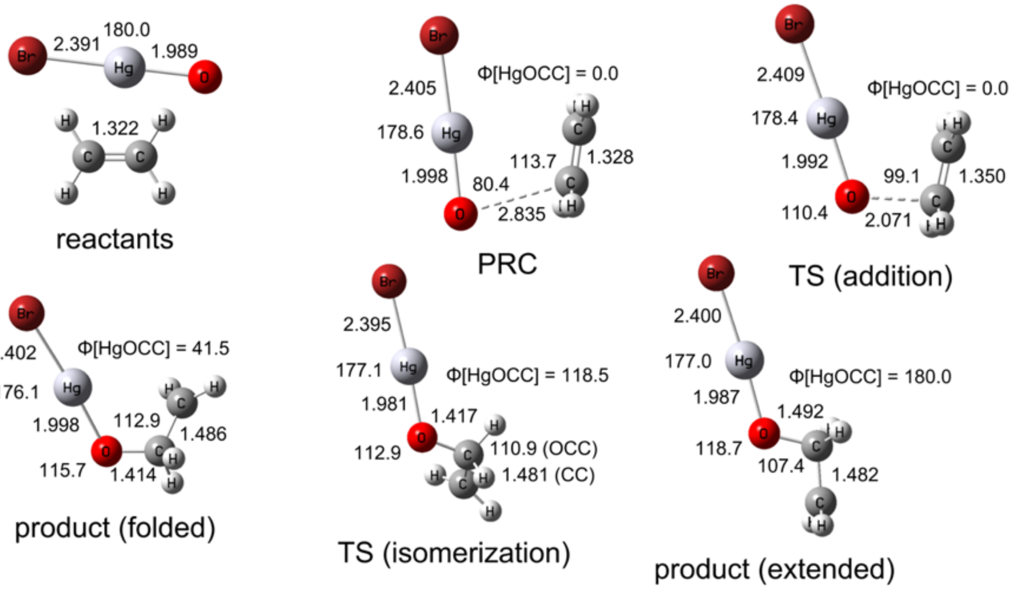

Figure 2. Reactants, products ($BrHgOCH_2CH_2\bullet$), and all saddle points of the $BrHgO\bullet + C_2H_4$ reaction at M06-2X/AVTZ. Product (folded) and TS (isomerization) possess C_1 symmetry, whereas all other species belong to the C_s point group. Distances are listed in Å and angles in degrees.

As introduced in the Methods section, the presence of a PRC divides the potential energy surface (PES) into two transition-state regions: an outer region corresponding to long-range interactions between the isolated fragments, and an inner region (related to the saddle point) where bonds between the fragments are formed.[42,43] As discussed elsewhere, in systems with a PRC and a submerged saddle point, the inner transition state generally gains importance as temperature increases, and vice versa, the outer transition state becomes more important as temperature decreases.[42] The effect of either transition state on reaction rate constants further depends on the depth of the PRC and the extent to which the inner transition state lies beneath the reactants. One may treat these systems using the unified statistical model (two-transition-state model),[44] which microcanonically accounts for the presence of multiple transition states along the same reaction path. Due to the unreliability of computed partition functions along the reaction paths near both transition-state regions (discussed below), we treated the transition states individually and considered the PRC as a local minimum on the PES in our Master Equation simulations.

We investigated the path containing the long-range transition state by performing a relaxed scan on the Hg–C bond distance of the PRC and computing vibrational frequencies perpendicular to the path. The left side of **Figure 3** displays the absolute energies, enthalpies at 298 K, and Gibbs free energies at 298 K (G) along the relaxed scan. Unfortunately, we found multiple maxima in G at large separations (5 Å < $r_{Hg\text{–}C}$ < 9 Å). These extreme spikes in the Gibbs free energy curve are not due to enthalpy and absolute energy changes, but instead a result of the values of some low-frequency modes changing between real and imaginary at various points along the path. One clearly sees this issue by comparing the positions of some G maxima at long Hg–C distances in **Figure 3** with the presence of one or more imaginary frequencies at that point in **Figure 4**.

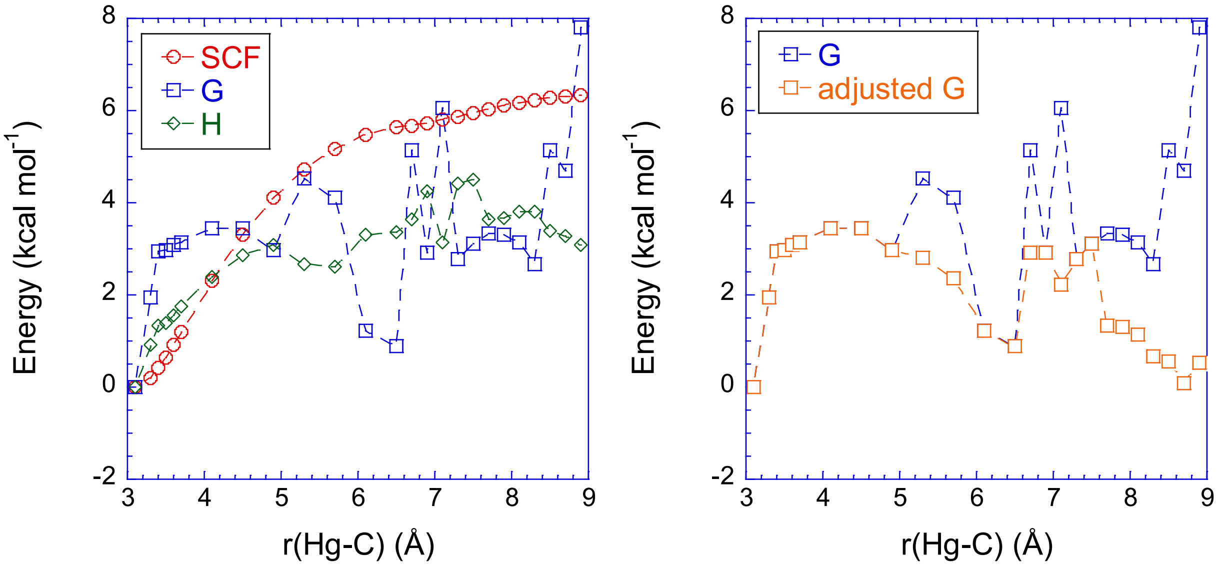

Figure 3. Left: absolute energies without ZPE (SCF, red circles), Gibbs free energies at 298 K (G, blue squares), and enthalpies at 298 K (H, green diamonds) relative to those at the PRC ($r_{Hg–C}$ ~ 3 Å) along the PRC-forming path for the reaction BrHgO• + C_2H_4 at M06-2X/AVTZ. Right: Gibbs free energies (blue squares, identical to blue squares on the left) and the adjusted Gibbs free energies (orange squares) at 298 K relative to that at the PRC. The adjusted free energies were computed by changing imaginary frequencies to the value of the non-imaginary frequency for the same mode at the nearest step (of lower $r_{Hg–C}$) on the reaction path.

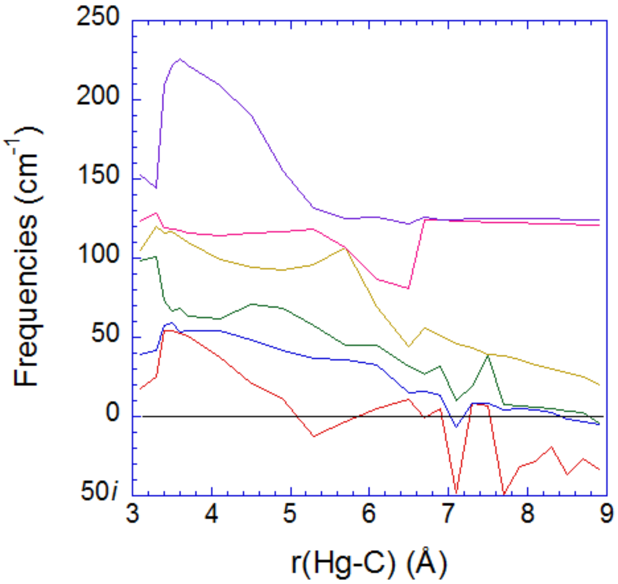

Figure 4. Harmonic frequencies of the six lowest vibrational modes along the PRC-forming path for the reaction BrHgO• + C_2H_4 at M06-2X/AVTZ. The black line at 0 cm^{-1} distinguishes between real and imaginary frequencies.

The magnitude of these imaginary frequencies remained essentially unchanged when we used tighter optimization criteria than the default, nor did they depend on whether we used ultrafine or default grids for calculating vibrational frequencies. Therefore, it seems that the imaginary frequencies did not arise from a lack of convergence or numerical instability. The issue of extra imaginary frequencies was discussed in a study of hydrogen abstraction by OH.[45] In that study, non-physical imaginary frequencies obtained on the MEP using a Cartesian coordinate system (as used in Gaussian) are largely eliminated by using redundant internal coordinates. We suspect the same approach might reduce or remove the non-physical imaginary frequencies observed in this work.

To determine if the issue persists at other levels of theory beside M06-2X, we optimized the PRC and carried out the relaxed scans using the PBE1PBE (PBE0) and MPW1PW91 functionals. These functionals were selected based on their success in previous calculations for structures and vibrational frequencies of mercury compounds.[46,47] Unfortunately, these scans ran into similar problems to those occurring at M06-2X. Curiously, these functionals yield different PRC geometries from M06-2X: PBE0 predicts a C_1 geometry, whereas MPW1PW91 produces a C_s geometry with the C=C bond of C_2H_4 perpendicular to the Hg–O bond. Geometries of the complexes computed at the various levels of theory are displayed in the Supporting Information (**Figure S2**). The presence of imaginary frequencies in the scans and the sensitivity of the PRC geometries to the level of theory both suggest the PES for forming the PRC to be quite flat.

Using the M06-2X scan left us with the issue of spurious maxima in G due to presence of imaginary frequencies at long separations. To minimize these artifacts, we changed the value of each imaginary frequency to the non-imaginary value for the same mode at the nearest step (of lower $r_{Hg–C}$) on the reaction path. In this manner we retained most of the entropy contribution of that mode to G at that step, and, therefore, largely removed the spike in G at that step of the MEP. The resulting adjusted free energy curve, displayed in **Figure 3** on the right side, has its most prominent maximum in G at $r_{Hg–C} \approx 4.5$ Å. It should be noted that the position of the maximum in G remains unchanged over the temperature range considered here. Despite the uncertainty in the Gibbs free energies, we decided to use this maximum to compute the temperature-dependent k^{VTST} for the PRC-forming step (values are provided in **Table S4** of the Supporting Information).

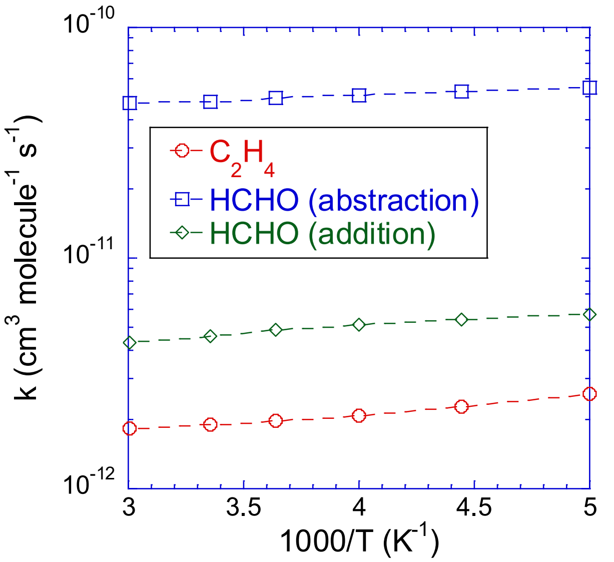

Figure 5. Effective second-order rate constants at 1 atm (*k*, in cm^3 molecule^{-1} s^{-1}) for the BrHgO• + C_2H_4 (red circles) and the BrHgO• + HCHO (blue squares and green diamonds, for hydrogen abstraction and addition, respectively) reactions at CCSD(T)//M06-2X/AVTZ.

The PRC-forming rate constants $k^{VTST}(T)$ stay relatively constant at 3.7 to 4.2 × 10^{-12} cm^3 molecule^{-1} s^{-1} (200 K ≤ *T* ≤ 333 K). Additionally, the fraction forming products from PRC decreases only moderately with increasing temperature from 0.65 to 0.44 but remains essentially unchanged (varying by < 1% at any given temperature) with changes in pressure over the range 0.01 atm ≤ *P* ≤ 1 atm. We briefly investigated the effect of tunneling by performing a simulation at 298 K with Eckart tunneling in the inner barrier for BrHgO• + C_2H_4. The inclusion of Eckart tunneling increased the fraction going to form product by ~2% (from 0.65 to 0.66). As a result, we do not include tunneling effects in results reported for BrHgO• + C_2H_4. Values of the PRC-forming rate constants $k^{VTST}(T)$, the fractions forming product *f*([M], *T*), and the effective rate constants *k*([M], *T*) are provided in **Table S4** of the Supporting Information. **Figure 5** displays *k*([M], *T*) for the BrHgO• + C_2H_4 reaction. The reaction rate constant varies from 1.8 to 2.6 × 10^{-12} cm^3 molecule^{-1} s^{-1} over the range of temperature and pressure in our simulations. By comparison, the experimental OH• + C_2H_4 rate constants are at least four times as high (8 × 10^{-12} cm^3 molecule^{-1} s^{-1} at 296 K and 1 atm),[48] and exhibit a strong negative temperature dependence (rising by a factor of 2 as the temperature decreases to 200 K at 1 atm). Our results therefore suggest that (1) BrHgO• adds to C_2H_4 slightly less favorably than does OH•, and (2) addition to C_2H_4 by BrHgO• has a weaker temperature and pressure dependence than addition by •OH. Experiments or more refined calculations would be needed to verify these conclusions.

In the BrHgO• + C_2H_4 system, both the PRC-forming rate constants and the efficiency of product formation are roughly independent of temperature. Pressure has a negligible effect on *f*([M], T) because both PRC dissociation and product formation largely occur prior to a single collision: at 298 K and 1 atm, 90% of the PRCs has reacted within the first 120 ps, whereas the PRCs have only had a 7% chance of undergoing a collision in this time. By contrast, *k*([M], T) for •OH + C_2H_4 exhibits a large pressure dependence, likely due to the smaller binding energy of the PRC as compared to the BrHgO• system. That being said, given the problems with the M06-2X frequencies in the long-range transition state region and, most importantly, the absence of experimental data with which we may evaluate our results, non-trivial uncertainties are expected for the computed BrHgO• + C_2H_4 rate constants. In this system, the two dominant sources of uncertainties are in (1) the height of the Gibbs Free Energy barrier ($\Delta G^{\dagger}(T)$) in the outer transition state region and (2) the barrier (E_{inner}) for product formation in the inner transition state region.

To study the combined effect of uncertainty in the saddle point energy and $\Delta G^{\dagger}$ for the outer transition state on BrHgO• + C_2H_4 rate constants, we carried out Master Equation simulations for the full range of temperatures (200 K $\leq T \leq$ 333 K) and pressures (0.01 atm $\leq$ P $\leq$ 1 atm) while varying E_{inner} up and down by 0.5 kcal mol^{-1}. We simultaneously varied the energy of the variational outer TS (E_{outer}) up and down by 0.5 kcal mol^{-1}, thereby varying the corresponding $\Delta G^{\dagger}(T)$ by the same amount at each temperature. This change in $\Delta G^{\dagger}$ affects both the PRC-forming rate constants $k^{\text{VTST}}(T)$ and the initial energy distribution of the chemically activated PRCs. By simultaneously varying E_{inner} and $\Delta G^{\dagger}$ for the outer TS, we explored a 3 × 3 matrix of possible values for each $k([\text{M}], T)$. **Table S5** displays all product-forming fractions and effective rate constants from this sensitivity analysis. Generally, the uncertainty in $\Delta G^{\dagger}$ has a stronger impact on the (effective) reaction rate constants than the inner critical energy. In the extreme case of 200 K, a shift by 0.5 kcal mol^{-1} in $\Delta G^{\dagger}$ changes $k([\text{M}], T)$ by a factor of 3, whereas a shift by the same amount in the inner barrier can cause the effective rate constants to change by only 40%. However, at the highest temperature studied here (T ≥ 298), the impacts on the rate constants become somewhat comparable. By contrast, in the •OH + C_2H_4 system, the rate constant at 300 K depends largely on the inner critical energy: an increase in the energy of the inner saddle point by 1.0 kcal mol^{-1} reduces the high-pressure effective rate constant by a factor of 5.[42] Maximum and minimum rate constants $k([\text{M}], T)$ computed in the sensitivity analysis at various temperatures are depicted in **Figure S3** of the Supporting Information.

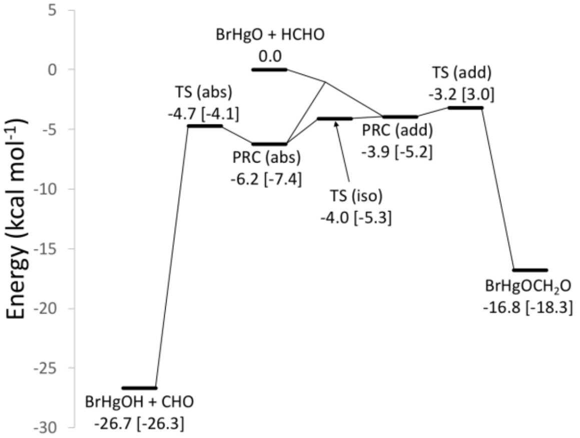

Figure 6. ZPE-corrected potential energy profile for the BrHgO• + HCHO reaction at CCSD(T)//M06-2X/AVTZ. Values in brackets are energies at M06-2X/AVTZ. The diverging path between the reactants and the PRCs signifies the point of bifurcation on the PES.

BrHgO• + HCHO reactions. Figure 6 displays the potential energy profile for the BrHgO• + HCHO reaction. The system possesses two channels: BrHgO• may either abstract a hydrogen atom to form BrHgOH or add to the carbon atom of HCHO to form BrHgOCH_2O•. Each channel contains a PRC, a submerged saddle point (by 4.7 kcal mol^{-1} and 3.2 kcal mol^{-1} at the CCSD(T) level of theory, respectively), and an exothermic product or product set. Note that for the analogous •OH + HCHO system, only abstraction occurs under atmospheric conditions, as the addition channel possesses a ~5 kcal mol^{-1} barrier.[49] **Figure 7** displays the structures of reactants, products, PRCs, and all saddle points of the BrHgO• + HCHO reaction. The two PRCs are connected to each other via a rotational saddle point, TS(isomerization).

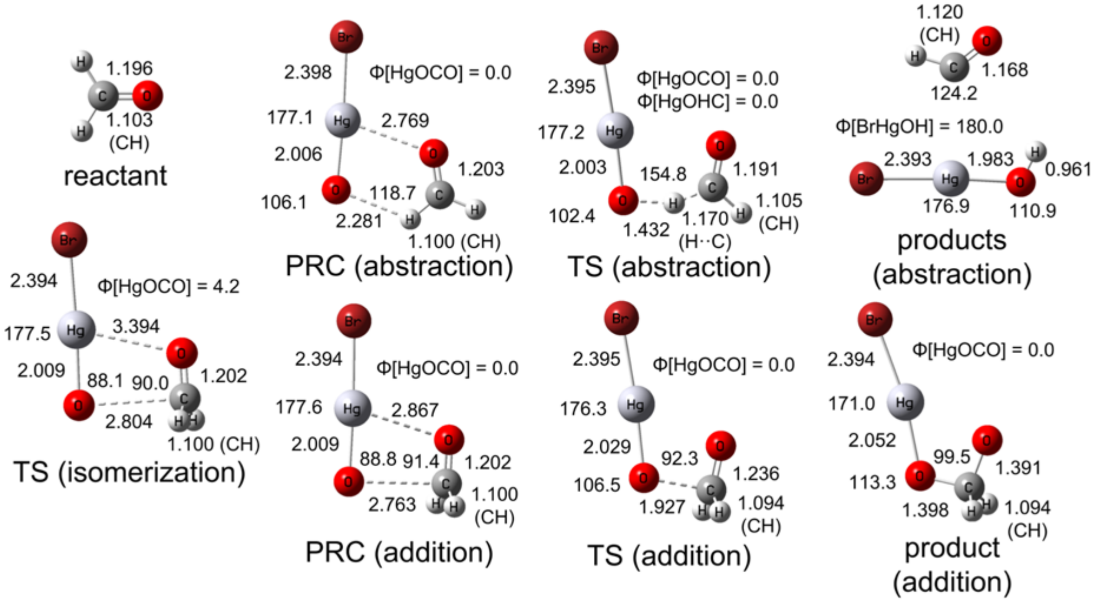

Figure 7. Reactants, products, and all saddle points of the BrHgO• + HCHO reaction at M06-2X/AVTZ. All species belong to the C_s point group, except for TS(isomerization) (C_1).

To map the reaction path connecting these PRCs to the isolated reactants, we performed relaxed scans of the bond distance between the Hg and the O of HCHO starting from each of the PRCs. **Figure 8** plots the resulting energies along the relaxed scan starting from the addition and abstraction PRCs, and displays geometries at a few points on the scan. The two reaction paths are the same for $r_{Hg-O} \geq 6.1$ Å. As the two reactants approach each other from large distances, BrHgO• lies collinear to the carbon and oxygen atoms of HCHO, and all the atoms are in the same plane (structures A and B). Once the paths diverge, BrHgO• internally rotates either (1) in this plane (structure C) to form the hydrogen abstraction PRC (PRC_{abs}) or (2) perpendicularly to this plane (structure D) to form the addition PRC (PRC_{add}). It should be noted that we were unable to identify a local minimum in the region where the paths split ($r_{Hg-O} \approx 6.1$ Å). The divergence of reaction paths without an intervening intermediate strongly points towards the existence of a bifurcating surface.[50] Bifurcations are commonly identified when the reaction paths are initially one and the same but diverge after overcoming an initial barrier (all within a one-step mechanism). In our case, the reaction path overcomes a variational transition state (as opposed to a saddle point) for approach of two reactants. Subsequently, the surface splits into two non-equivalent paths at the bifurcation point, each forming a distinct PRC leading to a different set of products. Generally, on a bifurcating surface, the shape of the PES and dynamics controls the branching ratios of product formation.[51] Due to the asymmetry of the PRC-forming reaction paths past the bifurcation point, they are not expected to be formed in equal proportions,[50] but the factors controlling product ratios in bifurcations are not yet fully understood.

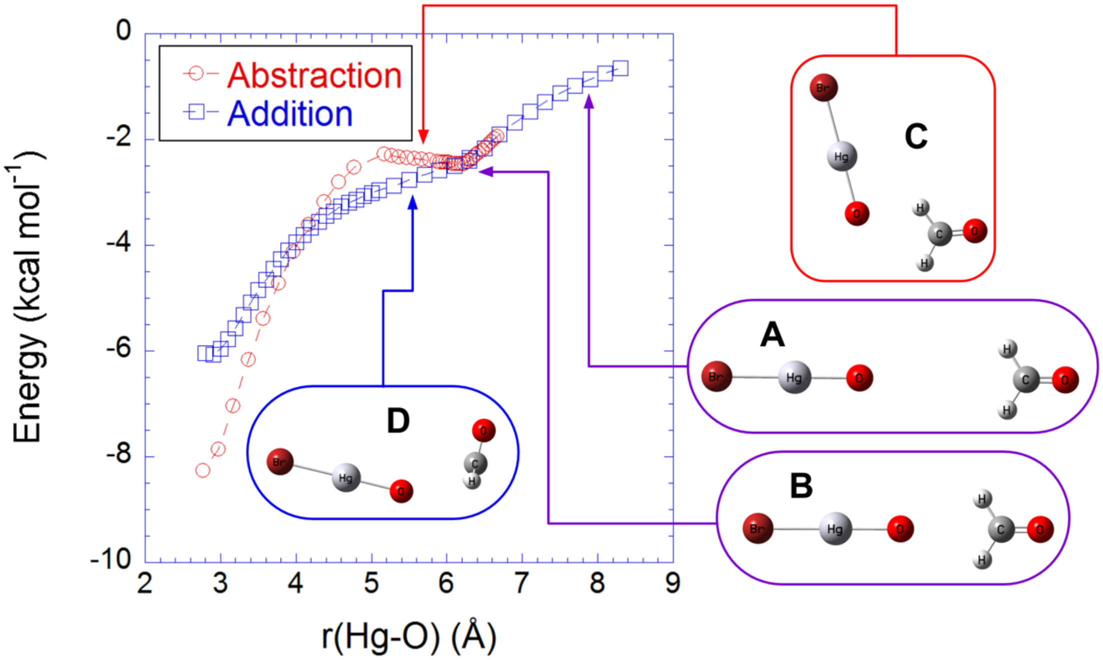

Figure 8. Relaxed scan on the Hg–OCH$_2$ internuclear distance along the hydrogen abstraction and addition PRC-forming paths at M06-2X/AVTZ for the BrHgO• + HCHO reaction. Reported energies are relative to that of the reactants ($r_{Hg–O} > 9$ Å). A few geometries along the path are displayed to illustrate the orientation of the reactants and the internal rotations leading to each PRC.

In contrast to many studied cases of bifurcation,[52–54] our work presents a bifurcating path towards PRCs as opposed to directly towards reaction products. The one previous work to study bifurcation on the analogous •OH + HCHO system[49] showed that the approaching •OH and HCHO form a single PRC, and the reaction path subsequently bifurcates into two superimposable mirror-image paths. In this case, the bifurcation affects the rate constants but not the structure of the products. Our BrHgO• + HCHO system differs from the analogous •OH + HCHO system in that it has two distinct PRCs, and each can be formed by two equivalent reaction paths (due to the symmetry of HCHO). Computing rate constants for the BrHgO• + HCHO system presents two challenges: (1) that the PRCs are not likely to exhibit fast IVR,[55–59] and (2) more generally, that determining the effect of the bifurcation would require expensive dynamical calculations. Given that our work presents the first-ever study on the BrHgO• + HCHO reaction, we decided to use only the long-range (pre-bifurcation-point) transition state as the rate-determining transition state for both PRC-forming steps. Our assumption that the rate-determining transition state precedes the bifurcation point seems common in the literature on bifurcation.[60–62] Additionally, reliably treating the PRC-forming path would require accounting for all dynamic effects in all paths, including around the saddle point by which the PRCs are connected to each other.

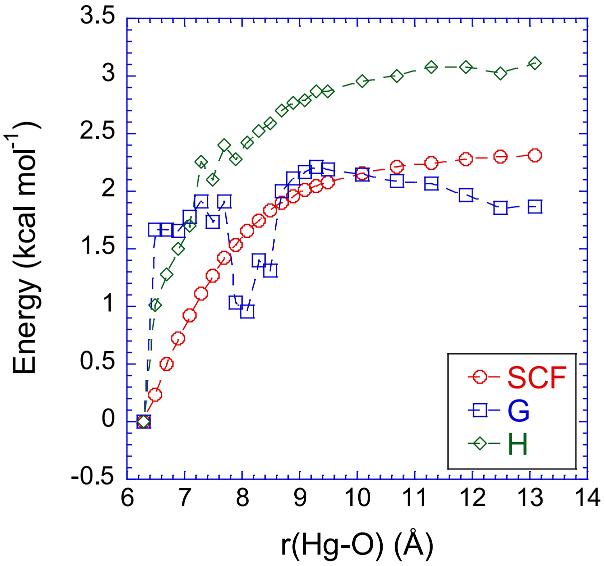

Figure 9. Absolute energies without ZPE (SCF, red circles), Gibbs free energies at 298 K (G, blue squares), and enthalpies at 298 K (H, green diamond) relative to those at the bifurcation point ($r_{Hg–C}$ ~ 6 Å) along the Hg–OCH_2 coordinate for the reaction of BrHgO• + HCHO at M06-2X/AVTZ.

To determine the k^{VTST} prior to the bifurcation point, we mapped out the Gibbs free energies at long Hg–O bond distances. **Figure 9** displays the Gibbs free energies at 298 K together with the absolute energies, and enthalpies (at 298 K) along the relaxed scan. Despite the jagged free energy curve, a maximum in G near $r_{Hg–O} \approx 9.3$ Å appears to be the variational transition state. Note that this long intermolecular distance arises from using Hg and O of HCHO for the relaxed scan; the BrHgO–C and BrHgO–H distances are much shorter. The spikes in the free energy curve, similar to those in the BrHgO• + C_2H_4 system, are correlated to the change in the values of some low-frequency modes from real to imaginary. These frequencies along the relaxed scan are available in the Supporting Information (**Figure S4**). We used the maximum in G near $r_{Hg–O} \approx 9.3$ Å to compute $k^{VTST}(T)$ for the PRC-forming steps in both channels. It should be noted that this position of the maximum in G does not change with temperature (200 K ≤ T ≤ 333 K). Over the same temperature range, $k^{VTST}(T)$ increases from 8.4×10^{-11} to 1.2×10^{-10} cm^3 molecule^{-1} s^{-1}. These rate constants are presented in the Supporting Information (**Table S7**).

As the two PRCs are connected to each other via a submerged barrier, they can isomerize, and the reaction can proceed via addition or abstraction regardless of the path the system follows past the bifurcation point (i.e., the identity of the PRC initially formed). Using Master Equation simulations, we studied the competition between these two channels by initially populating either PRC_{add} or PRC_{abs} (chemically activated) and allowing them to dissociate to reactants, isomerize, or react to form products during the simulation. Each simulation initiated from a given PRC produces a fractional yield for addition, f_{add}([M], T), and another for abstraction, f_{abs}([M], T) at a given temperature and pressure. If we assume, parsimoniously, that the two PRCs are formed in identical yields, the effective fraction reacting via addition at a given pressure and temperature, $f_{add,eff}$([M], T), is given by the average of the two f_{add}([M], T) computed for each initial population distribution. Likewise, the fraction proceeding via abstraction is given by the averaged f_{abs}([M], *T*). These effective fractional populations correspond to the branching ratios of the BrHgO• + HCHO reactions. The branching ratios are subsequently used to compute the effective bimolecular rate constant for each reaction channel (e.g., k_{add}([M], *T*) = $f_{\mathrm{add,eff}}$([M], *T*) × $k^{\mathrm{VTST}}(T)$). The fractions and the effective rate constants are available in the Supporting Information (**Table S7**). Regardless of PRC initially populated, the system proceeds via abstraction (f_{abs}([M], *T*) ~ 0.65 to 0.39) more than addition (f_{add}([M], *T*) ~ 0.06 to 0.03) at any given temperature and pressure, suggesting that the identity of the reaction products appears to be insensitive to the initial PRC branching ratios produced by the bifurcation. Note that tunneling was neglected in the results reported here; a simulation that included Eckart tunneling increased the fraction going to form product by < 2%.

Figure 5 displays the effective second-order rate constants for the BrHgO• + HCHO reactions at 1 atm. Hydrogen abstraction proceeds with a rate constant ten times higher than does addition at all temperatures and pressures. Furthermore, similar to our previous finding on BrHgO• hydrogen abstraction,[23] BrHgO• abstracts from HCHO with a higher rate constant than does •OH (4.8×10^{-11} cm^3 molecule^{-1} s^{-1} vs. 8.5×10^{-12} cm^3 molecule^{-1} s^{-1} at 298 K and 1 atm).[48]

As temperature increases from 200 K to 333 K, the fractions going to products via either channel decreases somewhat (from 0.65 to 0.39 for abstraction at 1 atm), counteracting the small increase in the PRC-forming rate constants. As a result, the effective rate constants of both BrHgO• + HCHO channels exhibit only a weak temperature dependence, staying relatively constant at 4.3 – 5.8×10^{-12} and 4.7 – 5.5×10^{-11} cm^3 molecule^{-1} s^{-1} for addition and abstraction, respectively. Pressure has a much smaller effect on these fractions (< 1% across $0.01 \text{ atm} \leq P \leq 1 \text{ atm}$ at any given temperature). Similarly, •OH + HCHO rate constants vary little over this temperature and pressure range.[48] As mentioned previously, the absence of experimental kinetic data hinders us from evaluating our results directly. These uncertainties include uncertainties in $\Delta G^{\dagger}$ for PRC formation, the critical energy for reaction product formation from PRCs, and the critical energy for isomerization between the PRCs.

To investigate some of the uncertainties in the rate constants of this system, we carried out Master Equation simulations while varying (1) the energy of the outer TS (E_{outer}) leading to the bifurcation up and down by 0.5 kcal mol^{-1}, thereby varying $\Delta G^{\dagger}$ for PRC formation by the same amount at each temperature; and (2) increasing the height of the (submerged) barrier for PRC isomerization by up to 1.0 kcal mol^{-1}. Fractions going on to form products for these simulations (averaged over the 50:50 initial population distribution of the two PRCs) are listed in the Supporting Information (**Table S8**). Rate constants are more sensitive to change in E_{outer} than in E_{iso}: a 0.5 kcal mol^{-1} shift in can induce a change in the reaction rate constant by a factor of ~2, whereas a shift in E_{iso} by the same amount only changes the rate constants by ~30%. Note that raising the barrier height for PRC-isomerization by 1.0 kcal mol^{-1} does not change the dominant behavior of the system: producing BrHgOH by hydrogen abstraction. These lines of evidence suggest that the uncertainty in the outer transition state region (i.e., before the PRCs are formed and where the bifurcation occurs) matters more to the BrHgO• + HCHO rate constants than the uncertainty in the inner region. Maximum and minimum rate constants *k*([M], *T*) for each reaction channel computed in the sensitivity analysis as a function of temperature are depicted in **Figure S5** of the Supporting Information. Additional uncertainty arises from the challenges of treating the bifurcation in this system.

ATMOSPHERIC IMPLICATIONS

Given the reactivity of BrHgO• with C_2H_4, we expect BrHgO• to add to larger alkenes and other compounds containing carbon-carbon double bonds. These compounds would include isoprene, the most abundantly emitted VOC, globally. By analogy to trends in rate constants for •OH addition to alkenes,[63] BrHgO• would react with isoprene with a higher rate constant than with C_2H_4.

The subsequent fate of $BrHgOCH_2CH_2$• would most likely be similar to that of other carbon-centered radicals: O_2 addition followed by reaction with NO or HO_2, as illustrated by **Scheme 1**. The formation of $BrHgOCH_2CH_2$•, its larger analogs (BrHgORZ• in **Figure 10**), and their subsequent reaction products represent conversion of inorganic Hg(II) compounds to organomercury species.

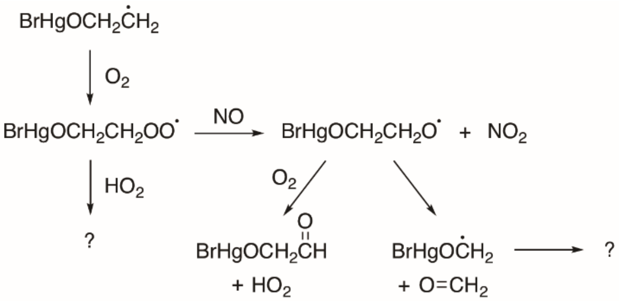

Scheme 1. Predicted fate of $BrHgOCH_2CH_2$• by analogy to $HOCH_2CH_2$•.

For the BrHgO• + HCHO mechanism shown in **Scheme 1**, the alkoxy radical product intermediate, $BrHgOCH_2O$•, may lose a hydrogen atom to form an aldehyde, either unimolecularly or via bimolecular reaction with O_2:

$$BrHgOCH_2O\bullet \rightarrow BrHgOCH{=}O + H\bullet \qquad (12)$$

$$BrHgOCH_2O\bullet + O_2 \rightarrow BrHgOCH{=}O + HO_2\bullet \qquad (13)$$

However, due to the dominance of the hydrogen abstraction rate constants, the BrHgO• reaction with aldehydes primarily represents a source of BrHgOH. BrHgO• reaction with ketones (as opposed to aldehydes) may be a more important source of alkoxy radicals with BrHgO substituent. Note that larger alkoxy radicals, including analogs of the $BrHgOCH_2CH_2O$• intermediate in Scheme 1, would likely undergo more diverse chemistry than is depicted above.[64,65]

Considering the toxicity of organomercury compounds,[4,66] their formation in the gas phase via addition to carbonyl compounds and alkenes may appear disconcerting. Nonetheless, as detailed below, we expect most BrHgO• to form BrHgOH, so these organomercury compounds may not be cause for alarm. The fate of BrHgOH was previously suggested to be wet and dry deposition,[23] or photolysis.[24]

All in all, BrHgO• behaves similarly to •OH radical, in that it can abstract hydrogen atoms from sp^3-hydridized carbons atoms, and can add to sp^2-hybridized carbons, and to NO and NO_2.[23] These reactions are depicted in **Figure 10** in the context of bromine-initiated oxidation of Hg(0). Additionally, we expect that BrHgO• can add to aromatic compounds, although we have yet to investigate these reactions.

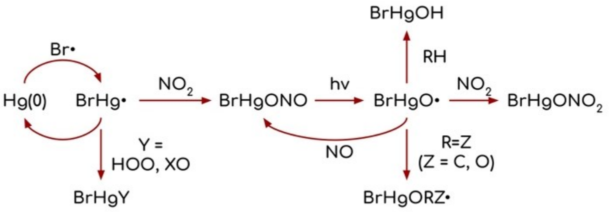

Figure 10. Mechanism of Hg(0) oxidation initiated by Br• including the various reactions of BrHgO•.

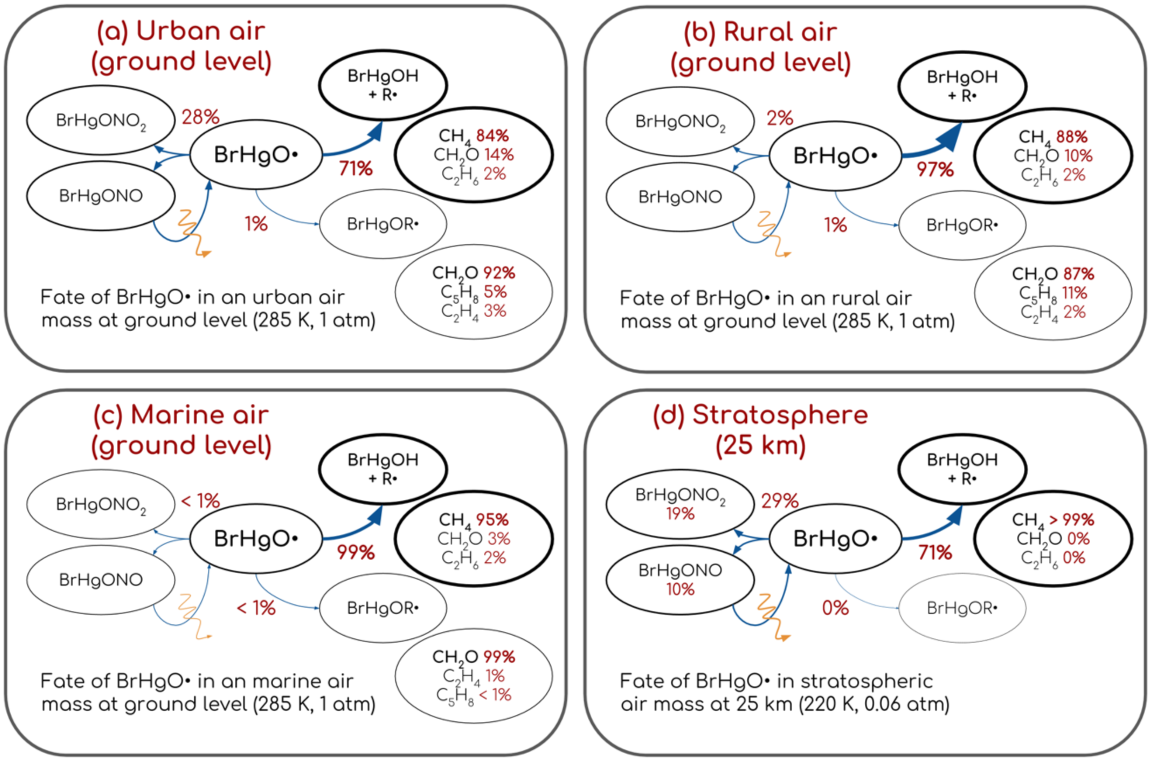

Figure 11. Predicted fates of BrHgO• in three air masses at ground level (a, b, and c) and one in the stratosphere (d). Values are calculated from pseudo first-order rate constants ($k'_A = k[A]$ where k is the bimolecular rate constant for reaction BrHgO• reacting with compound A computed at CCSD(T)//M06-2X/AVTZ). Concentration values are adapted from data obtained in field campaigns and listed in the Supporting Information (**Table S9**).

Finally, we estimate the atmospheric fate of BrHgO• under a variety of conditions by computing pseudo first-order rate constants of its reactions ($k'_A = k[A]$ where k is the bimolecular rate constant for reaction of BrHgO• with compound A). These values are computed for four air masses representing stratospheric air and lower-tropospheric air in urban, rural, and marine environments using concentration data from selected field campaigns. The concentrations are listed in the Supporting Information (**Table S9**). We included previously studied hydrogen abstractions from alkanes along with NO and NO_2 addition.[23] **Figure 11** displays the predicted fates of BrHgO• in these four air masses. BrHgOH formation dominates in all air masses due to the high global concentration of CH_4. However, addition to nitrogen oxides can compete in urban regions and in stratospheric air. Photolysis of BrHgONO, and perhaps, $BrHgONO_2$, provides a channel whereby BrHgO• can be regenerated. Two factors limit the reliability of the results in **Figure 11**: (1) that these rate constants are uncertain and require verification from experiments, and (2) that we only include a few species and reactions whose rate constants were computed. That being said, it seems likely that BrHgOH constitutes a major Hg(II) compound formed in the bromine-initiated oxidation of Hg(0). We hope that these results inspire experimentalists to refine the rate constants reported here.

SUPPORTING INFORMATION

Tables of absolute energies, ZPEs, Cartesian coordinates, vibrational frequencies, and rotational constants for all species are available in the Supporting Information. Tables of temperature-dependent PRC-forming rate constants, fractions reacting to form products, effective rate constants, along with figures of Gibbs free energies and vibrational frequencies along reaction paths are also presented. In addition, atmospheric concentrations and rate constants used for predicting the fate of BrHgO• are included.

AUTHOR INFORMATION

*Corresponding author: tsdibble@esf.edu

ACKNOWLEDGEMENT

We thank the National Science Foundation for their support of the present work under award number 1609848. The project used computing resources at Extreme Science and Engineering Discovery Environment (XSEDE), supported by the National Science Foundation grant number ACI-1053575; in particular, we used the Comet cluster at the San Diego Supercomputing Center (SDSC) and the Bridges system at the Pittsburgh Supercomputing Center (PSC). We particularly appreciate the many thoughtful comments of one of the anonymous reviewers.

REFERENCES

(1) Driscoll, C. T.; Mason, R. P.; Chan, H. M.; Jacob, D. J.; Pirrone, N. Mercury as a Global Pollutant: Sources, Pathways, and Effects. *Environ. Sci. Technol.* **2013**, *47* (10), 4967–4983.

(2) Lin, C.-J.; Pehkonen, S. O. The Chemistry of Atmospheric Mercury: A Review. *Atmos. Environ.* **1999**, *33* (13), 2067–2079.

(3) Schroeder, W. H.; Munthe, J. Atmospheric Mercury—An Overview. *Atmos. Environ.* **1998**, *32* (5), 809–822.

(4) Mergler, D.; Anderson, H. A.; Chan, L. H. M.; Mahaffey, K. R.; Murray, M.; Sakamoto, M.; Stern, A. H.; Panel on Health Risks and Toxicological Effects of Methylmercury. Methylmercury Exposure and Health Effects in Humans: A Worldwide Concern. *Ambio* **2007**, *36* (1), 3–11.

(5) Lin, C.-J.; Pongprueksa, P.; Russell Bullock, O.; Lindberg, S. E.; Pehkonen, S. O.; Jang, C.; Braverman, T.; Ho, T. C. Scientific Uncertainties in Atmospheric Mercury Models II: Sensitivity Analysis in the CONUS Domain. *Atmos. Environ.* **2007**, *41* (31), 6544–6560.

(6) Travnikov, O.; Angot, H.; Artaxo, P.; Bencardino, M.; Bieser, J.; Amore, F.; Dastoor, A.; De Simone, F.; Diéguez, M. del C.; Dommergue, A.; et al. Multi-Model Study of Mercury Dispersion in the Atmosphere: Atmospheric Processes and Model Evaluation. *Atmos. Chem. Phys.* **2017**, *17* (8), 5271–5295.

(7) Sprovieri, F.; Pirrone, N.; Bencardino, M.; Amore, F.; Carbone, F.; Cinnirella, S.; Mannarino, V.; Landis, M.; Ebinghaus, R.; Weigelt, A.; et al. Atmospheric Mercury Concentrations Observed at Ground-Based Monitoring Sites Globally Distributed in the Framework of the GMOS Network. *Atmos. Chem. Phys.* **2016**, *16* (18), 11915–11935.

(8) Ye, Z.; Mao, H.; Driscoll, C. T.; Wang, Y.; Zhang, Y.; Jaeglé, L. Evaluation of CMAQ Coupled with a State-of-the-Art Mercury Chemical Mechanism (CMAQ-NewHg-Br). *J. Adv. Model. Earth Syst.* **2018**, *10* (3), 668–690.

(9) Wang, S.; Schmidt, J. A.; Baidar, S.; Coburn, S.; Dix, B.; Koenig, T. K.; Apel, E.; Bowdalo, D.; Campos, T. L.; Eloranta, E.; et al. Active and Widespread Halogen Chemistry in the Tropical and Subtropical Free Troposphere. *Proc. Natl. Acad. Sci. U. S. A.* **2015**, *112* (30), 9281–9286.

(10) Custard, K. D.; Thompson, C. R.; Pratt, K. A.; Shepson, P. B.; Liao, J.; Huey, L. G.; Orlando, J. J.; Weinheimer, A. J.; Apel, E.; Hall, S. R.; et al. The NO_x Dependence of Bromine Chemistry in the Arctic Atmospheric Boundary Layer. *Atmos. Chem. Phys.* **2015**, *15* (18), 10799–10809.

(11) Steffen, A.; Douglas, T.; Amyot, M.; Ariya, P.; Aspmo, K.; Berg, T.; Bottenheim, J.; Brooks, S.; Cobbett, F.; Dastoor, A.; et al. A Synthesis of Atmospheric Mercury Depletion Event Chemistry in the Atmosphere and Snow. *Atmos. Chem. Phys.* **2008**, *8* (6), 1445–1482.

(12) Horowitz, H. M.; Jacob, D. J.; Zhang, Y.; Dibble, T. S.; Slemr, F.; Amos, H. M.; Schmidt, J. A.; Corbitt, E. S.; Marais, E. A.; Sunderland, E. M. A New Mechanism for Atmospheric Mercury Redox Chemistry: Implications for the Global Mercury Budget. *Atmos. Chem. Phys* **2017**, *17*, 6353–6371.

(13) Holmes, C. D.; Jacob, D. J.; Yang, X. Global Lifetime of Elemental Mercury against

Oxidation by Atomic Bromine in the Free Troposphere. *Geophys. Res. Lett.* **2006**, *33* (20), L20808.

(14) Ariya, P. A.; Khalizov, A.; Gidas, A. Reactions of Gaseous Mercury with Atomic and Molecular Halogens: Kinetics, Product Studies, and Atmospheric Implications. *J. Phys. Chem. A* **2002**, *106* (32), 7310–7320.

(15) Goodsite, M. E.; Plane, J. M. C.; Skov, H. A Theoretical Study of the Oxidation of Hg^0 to $HgBr_2$ in the Troposphere. *Environ. Sci. Technol.* **2004**, *38* (6), 1772–1776.

(16) Goodsite, M. E.; Plane, J. M. C.; Skov, H. Correction to A Theoretical Study of the Oxidation of Hg^0 to $HgBr_2$ in the Troposphere. *Environ. Sci. Technol.* **2012**, *46* (9), 5262–5262.

(17) Shepler, B. C.; Balabanov, N. B.; Peterson, K. A. Hg + Br → HgBr Recombination and Collision-Induced Dissociation Dynamics. *J. Chem. Phys.* **2007**, *127* (16), 164304.

(18) Wilcox, J.; Okano, T. Ab Initio-Based Mercury Oxidation Kinetics via Bromine at Postcombustion Flue Gas Conditions. *Energy & Fuels* **2011**, *25* (4), 1348–1356.

(19) Dibble, T. S.; Zelie, M. J.; Mao, H. Thermodynamics of Reactions of ClHg and BrHg Radicals with Atmospherically Abundant Free Radicals. *Atmos. Chem. Phys. Chem. Phys. Discuss* **2012**, *12* (21), 10271–10279.

(20) Jiao, Y.; Dibble, T. S. First Kinetic Study of the Atmospherically Important Reactions BrHg• + NO_2 and BrHg• + HOO. *Phys. Chem. Chem. Phys.* **2017**, *19* (3), 1826–1838.

(21) Jiao, Y.; Dibble, T. S. Structures, Vibrational Frequencies, and Bond Energies of the BrHgOX and BrHgXO Species Formed in Atmospheric Mercury Depletion Events. *J. Phys. Chem. A* **2017**, *121* (41), 7976–7985.

(22) Dibble, T. S.; Schwid, A. C. Thermodynamics Limits the Reactivity of BrHg• Radical with Volatile Organic Compounds. *Chem. Phys. Lett.* **2016**, *659*, 289–294.

(23) Lam, K. T.; Wilhelmsen, C. J.; Schwid, A. C.; Jiao, Y.; Dibble, T. S. Computational Study on the Photolysis of BrHgONO and the Reactions of BrHgO• with CH_4, C_2H_6, NO, and NO_2: Implications for Formation of Hg(II) Compounds in the Atmosphere. *J. Phys. Chem. A* **2019**, *123* (8), 1637–1647.

(24) Saiz-Lopez, A.; Sitkiewicz, S. P.; Roca-Sanjuán, D.; Oliva-Enrich, J. M.; Dávalos, J. Z.; Notario, R.; Jiskra, M.; Xu, Y.; Wang, F.; Thackray, C. P.; et al. Photoreduction of Gaseous Oxidized Mercury Changes Global Atmospheric Mercury Speciation, Transport and Deposition. *Nat. Commun.* **2018**, *9* (1), 4796–4805.

(25) Balabanov, N. B.; Peterson, K. A. Mercury and Reactive Halogens: The Thermochemistry of Hg + {Cl_2 , Br_2 , BrCl, ClO, and BrO}. *J. Phys. Chem. A* **2003**, *107* (38), 7465–7470.

(26) Frisch, M. J.; Trucks, G. W.; Schlegel, H. B.; Scuseria, G. E.; Robb, M. A.; Cheeseman, J. R.; Scalmani, G.; Barone, V.; Petersson, G. A.; Nakatsuji, H.; et al. Gaussian 09, Revision D.01. Gaussian, Inc.: Wallingford, CT 2016.

(27) Dunning, T. H. Gaussian Basis Sets for Use in Correlated Molecular Calculations. I. The Atoms Boron through Neon and Hydrogen. *J. Chem. Phys.* **1989**, *90* (2), 1007–1023.

(28) Kendall, R. A.; Dunning, T. H.; Harrison, R. J. Electron Affinities of the First-row Atoms

Revisited. Systematic Basis Sets and Wave Functions. *J. Chem. Phys.* **1992**, *96* (9), 6796–6806.

(29) Peterson, K. A.; Shepler, B. C.; Figgen, D.; Stoll, H. On the Spectroscopic and Thermochemical Properties of ClO, BrO, IO, and Their Anions. *J. Phys. Chem. A* **2006**, *110* (51), 13877–13883.

(30) Peterson, K. A.; Puzzarini, C. Systematically Convergent Basis Sets for Transition Metals. II. Pseudopotential-Based Correlation Consistent Basis Sets for the Group 11 (Cu, Ag, Au) and 12 (Zn, Cd, Hg) Elements. *Theor. Chem. Acc.* **2005**, *114* (4–5), 283–296.

(31) Zhao, Y.; Truhlar, D. G. The M06 Suite of Density Functionals for Main Group Thermochemistry, Thermochemical Kinetics, Noncovalent Interactions, Excited States, and Transition Elements: Two New Functionals and Systematic Testing of Four M06-Class Functionals and 12 Other Function. *Theor. Chem. Acc.* **2008**, *120* (1–3), 215–241.

(32) Raghavachari, K.; Trucks, G. W.; Pople, J. A.; Head-Gordon, M. A Fifth-Order Perturbation Comparison of Electron Correlation Theories. *Chem. Phys. Lett.* **1989**, *157* (6), 479–483.

(33) Barker, J. R. Multiple-Well, Multiple-Path Unimolecular Reaction Systems. I. MultiWell Computer Program Suite. *Int. J. Chem. Kinet.* **2001**, *33* (4), 232–245.

(34) Barker, J. R. Energy Transfer in Master Equation Simulations: A New Approach. *Int. J. Chem. Kinet.* **2009**, *41* (12), 748–763.

(35) Forst, W. *Unimolecular Reactions: A Concise Introduction*; Cambridge University Press, 2003.

(36) Yang, L.; Sonk, J. A.; Barker, J. R. HO + OClO Reaction System: Featuring a Barrierless Entrance Channel with Two Transition States. *J. Phys. Chem. A* **2015**, *119* (22), 5723–5731.

(37) Gilbert, R. G.; Smith, S. C. *Theory of Unimolecular and Recombination Reactions*; Blackwell Scientific: Oxford, UK, 1990.

(38) Shannon, R. J.; Caravan, R. L.; Blitz, M. A.; Heard, D. E. A Combined Experimental and Theoretical Study of Reactions between the Hydroxyl Radical and Oxygenated Hydrocarbons Relevant to Astrochemical Environments. *Phys. Chem. Chem. Phys.* **2014**, *16* (8), 3466–3478.

(39) Ali, M. A.; Sonk, J. A.; Barker, J. R. Predicted Chemical Activation Rate Constants for HO_2 + CH_2NH: The Dominant Role of a Hydrogen-Bonded Pre-Reactive Complex. *J. Phys. Chem. A* **2016**, *120* (36), 7060–7070.

(40) Long, B.; Bao, J. L.; Truhlar, D. G. Atmospheric Chemistry of Criegee Intermediates: Unimolecular Reactions and Reactions with Water. *J. Am. Chem. Soc.* **2016**, *138* (43), 14409–14422.

(41) Sleiman, C.; González, S.; Klippenstein, S. J.; Talbi, D.; El Dib, G.; Canosa, A. Pressure Dependent Low Temperature Kinetics for CN + CH_3CN: Competition between Chemical Reaction and van Der Waals Complex Formation. *Phys. Chem. Chem. Phys.* **2016**, *18* (22), 15118–15132.

(42) Greenwald, E. E.; North, S. W.; Georgievskii, Y.; Klippenstein, S. J. A Two Transition State Model for Radical−Molecule Reactions: A Case Study of the Addition of OH to C_2H_4. *J. Phys. Chem. A* **2005**, *109* (27), 6031–6044.

(43) Greenwald, E. E.; North, S. W.; Georgievskii, Y.; Klippenstein, S. J. A Two Transition State

Model for Radical−Molecule Reactions: Applications to Isomeric Branching in the OH−Isoprene Reaction. *J. Phys. Chem. A* **2007**, *111* (25), 5582–5592.

(44) Miller, W. H. Unified Statistical Model for "Complex" and "Direct" Reaction Mechanisms. *J. Chem. Phys.* **1976**, *65* (6), 2216–2223.

(45) Ellingson, B. A.; Pu, J.; Lin, H.; Zhao, Y.; Truhlar, D. G. Multicoefficient Gaussian-3 Calculation of the Rate Constant for the OH + CH_4 Reaction and Its $^{12}C/^{13}C$ Kinetic Isotope Effect with Emphasis on the Effects of Coordinate System and Torsional Treatment. *J. Phys. Chem. A* **2007**, *111* (45), 11706–11717.

(46) Montero-Campillo, M. M.; Lamsabhi, A. M.; Mó, O.; Yáñez, M. Alkyl Mercury Compounds: An Assessment of DFT Methods. *Theor. Chem. Acc.* **2013**, *132* (3), 1328.

(47) Jiao, Y.; Dibble, T. S. Quality Structures, Vibrational Frequencies, and Thermochemistry of the Products of Reaction of BrHg• with NO_2 , HO_2 , ClO, BrO, and IO. *J. Phys. Chem. A* **2015**, *119* (42), 10502–10510.

(48) Burkholder, J. B.; Sander, S. P.; Abbatt, J.; Barker, J. R.; Huie, R. E.; Kolb, C. E.; Kurylo, M. J.; Orkin, V. L.; Wilmouth, M. D.; Wine, P. H. Chemical Kinetics and Photochemical Data for Use in Atmospheric Studies, Evaluation No. 18. JPL Publication 15-10, Jet Propulsion Laboratory, Pasadena. 2015.

(49) Akbar Ali, M.; Barker, J. R. Comparison of Three Isoelectronic Multiple-Well Reaction Systems: OH + CH_2O, OH + CH_2CH_2, and OH + CH_2NH. *J. Phys. Chem. A* **2015**, *119* (28), 7578–7592.

(50) Rehbein, J.; Wulff, B. Chemistry in Motion—off the MEP. *Tetrahedron Lett.* **2015**, *56* (50), 6931–6943.

(51) Ess, D. H.; Wheeler, S. E.; Iafe, R. G.; Xu, L.; Celebi-Olçüm, N.; Houk, K. N. Bifurcations on Potential Energy Surfaces of Organic Reactions. *Angew. Chem. Int. Ed. Engl.* **2008**, *47* (40), 7592–7601.

(52) Mandal, N.; Datta, A. Dynamical Effects along the Bifurcation Pathway Control Semibullvalene Formation in Deazetization Reactions. *J. Phys. Chem. B* **2018**, *122* (3), 1239–1244.

(53) Villar, R.; López, L.; Faza, O. N.; Silva, C. Dynamic Effects Responsible for High Selectivity in a [3,3] Sigmatropic Rearrangement Featuring a Bispericyclic Transition State. *J. Org. Chem.* **2017**, *82* (9), 4758–4765.

(54) Hare, S. R.; Hudson, B. M.; Tantillo, D. J. Modeling Organic Reactions — General Approaches, Caveats, and Concerns. In *Applied Theoretical Organic Chemistry*; World Scientific: Europe, 2018; pp 1–29.

(55) Miller, R. E. The Vibrational Dynamics of Hydrogen Bonded Molecular Complexes at the State-to-State Level. In *Dynamics of Polyatomic Van der Waals Complexes*; Springer: New York, NY, 1990; pp 33–42.

(56) Huang, Z. S.; Miller, R. E. High-resolution Near-infrared Spectroscopy of Water Dimer. *J. Chem. Phys.* **1989**, *91* (11), 6613–6631.

(57) Merritt, J. M.; Rudić, S.; Miller, R. E. Infrared Laser Spectroscopy of $CH_3\cdots HF$ in Helium Nanodroplets: The Exit-Channel Complex of the $F+CH_4$ Reaction. *J. Chem. Phys.* **2006**, *124* (8), 084301.

(58) Morrison, A. M.; Flynn, S. D.; Liang, T.; Douberly, G. E. Infrared Spectroscopy of $(HCl)_m(H_2O)_n$ Clusters in Helium Nanodroplets: Definitive Assignments in the HCl Stretch Region. *J. Phys. Chem. A* **2010**, *114* (31), 8090–8098.

(59) Huneycutt, A. J.; Stickland, R. J.; Hellberg, F.; Saykally, R. J. Infrared Cavity Ringdown Spectroscopy of Acid–Water Clusters: $HCl–H_2O$, $DCl–D_2O$, and $DCl–(D_2O)_2$. *J. Chem. Phys.* **2003**, *118* (3), 1221–1229.

(60) Katori, T.; Itoh, S.; Sato, M.; Yamataka, H. Reaction Pathways and Possible Path Bifurcation for the Schmidt Reaction. *J. Am. Chem. Soc.* **2010**, *132* (10), 3413–3422.

(61) Castaño, O.; Frutos, L.-M.; Palmeiro, R.; Notario, R.; Andrés, J.-L.; Gomperts, R.; Blancafort, L.; Robb, M. A. The Valence Isomerization of Cyclooctatetraene to Semibullvalene. *Angew. Chemie Int. Ed.* **2000**, *39* (12), 2095–2097.

(62) Sandhiya, L.; Kolandaivel, P.; Senthilkumar, K. Depletion of Atmospheric Ozone by Nitrogen Dioxide: A Bifurcated Reaction Pathway. *Theor. Chem. Acc.* **2013**, *132* (9), 1382.

(63) Atkinson, R. Kinetics and Mechanisms of the Gas-Phase Reactions of the Hydroxyl Radical with Organic Compounds under Atmospheric Conditions. *Chem. Rev.* **1986**, *86* (1), 69–201.

(64) Dibble, T. S.; Chai, J. Critical Review of Atmospheric Chemistry of Alkoxy Radicals. In *Advances in Atmospheric Chemistry*; World Scientific, 2017; pp 185–269.

(65) Atkinson, R. Rate Constants for the Atmospheric Reactions of Alkoxy Radicals: An Updated Estimation Method. *Atmos. Environ.* **2007**, *41* (38), 8468–8485.

(66) Risher, J. F.; Murray, H. E.; Prince, G. R. Organic Mercury Compounds: Human Exposure and Its Relevance to Public Health. *Toxicol. Ind. Health* **2002**, *18* (3), 109–160.

TOC GRAPHIC